Experimental identification of distributed nonlinearities in the modal domain

D. Anastasio[1], S. Marchesiello[1], G. Kerschen[2], J.P. Noël[2]

[1]*Department of Mechanical and Aerospace Engineering, Politecnico di Torino, Corso Duca degli Abruzzi 24, 10129 Torino, Italy.*

[2]*Space Structures and Systems Laboratory, Department of Aerospace and Mechanical Engineering, University of Liège, Allée de la découverte 9, 4000 Liège, Belgium.*

https://doi.org/10.1016/j.jsv.2019.07.005

Cite as:

D. Anastasio, S. Marchesiello, G. Kerschen, J.P. Noël, Experimental identification of distributed nonlinearities in the modal domain, J. Sound Vib. 458 (2019) 426–444. doi:10.1016/j.jsv.2019.07.005.

Experimental identification of distributed nonlinearities in the modal domain

D. Anastasio[1], S. Marchesiello[1], G. Kerschen[2], J.P. Noël[2]

[1]*Department of Mechanical and Aerospace Engineering, Politecnico di Torino, Corso Duca degli Abruzzi 24, 10129 Torino, Italy.*

[2]*Space Structures and Systems Laboratory, Department of Aerospace and Mechanical Engineering, University of Liège, Allée de la découverte 9, 4000 Liège, Belgium.*

Abstract

This paper deals with the nonlinear system identification of structures exhibiting distributed nonlinearities, which has become of great interest recently, due to the continuous interest to improve the performance of structures. This brings the need for designing lighter and more flexible structural elements, which are usually characterized by moderate and large deformation, resulting in a distributed nonlinear behavior. In this framework, system identification remains a particularly challenging problem, especially when experimental measurements are considered. This work proposes a method to perform such a task, based on a convenient model order reduction of the considered structure, followed by a nonlinear system identification algorithm. The methodology is validated on a very thin beam undergoing large-amplitude oscillations, firstly using numerical data and then considering an experimental test bench. On the experimental side, the nonlinearity is first characterized using just the measured data, in order to acquire information that would help the identification process. Eventually, nonlinear system identification is performed in the reduced-order domain. An ad-hoc version of the nonlinear subspace identification (NSI) algorithm is used, but the presented methodology can also be applied with other nonlinear identification tools. Results confirm the goodness of the identification strategy in obtaining a reliable model which takes into account the distributed nonlinear behavior.

Keywords: nonlinear system identification; distributed nonlinearity; subspace identification; nonlinear beam; large deformations

1. Introduction

The study of large-amplitude vibrations of mechanical structures has a long tradition, especially when considering the mathematical modeling and the finite element representation. The reader can refer to the work of A.H. Nayfeh and P.F. Pai [1] for an extensive literature review about nonlinear beams, plates and shells. Despite this being a known phenomenon, the importance of dealing with geometrical nonlinearity has increased in the last years, becoming a key aspect to consider in the design and analysis of many structural applications, such as helicopter blades, large wind turbines, deployable solar panels, antennas for space applications and cylindrical shells [2,3].

Generally, geometrical nonlinearity arises when a structure undergoes large-amplitude vibrations, resulting in a distributed nonlinear strain-displacement relation [4]. In the case of thin-walled structures, this creates a coupling between bending and in-plane stretching deformations. The resulting dynamical behavior is then nonlinear, including hardening/softening effects and modal interactions. In this framework, a nonlinear model is very often obtained by projecting the physical domain onto a reduced-order basis, forming a reduced-order model [5]. Clearly, choosing the right projection basis is a key step to obtain a reliable model for the considered application. A well-known choice from the linear theory consists in considering the linear normal modes (LNMs) as a projection space. For nonlinear systems, such an approach has some limitations, because LNMs do not decouple the equations of motion and are able to reproduce the motion for moderately large amplitudes of vibrations only [6]. Other possibilities are the use of nonlinear normal modes and modal derivatives [6], which enrich the projection space allowing a more complete nonlinear model. Whatever reduced-order basis is used, the model parameters should then be retrieved, and this is done in the present work starting from experimental data.

While the existing literature on numerical studies about large-amplitude vibrations is quite rich, the same cannot be stated when experimental measurements are considered. Indeed, identifying a reliable model from experimental data is always a challenging task, and this is particularly true when the structure behaves nonlinearly. Several methods have been developed in the last decades to identify nonlinear dynamical structures with localized nonlinearities, and the reader can refer to [7,8] for an extensive literature review. The different methods are generally based on different assumptions, but they are generally not meant to work in the case of a distributed nonlinear behavior. A few recent works deal with this problem, but their application

is generally restricted to harmonic excitations under the assumption of no modal couplings. In [9] the experimental identification of a beam undergoing large-amplitude vibrations is reported, considering the first bending mode and fitting the nonlinear frequency response function (FRF) via harmonic balance method. In [10] an experimental diesis-like structure showing a geometrical nonlinear behavior is considered, and its model parameters estimated under the assumption of no internal resonances fitting again the nonlinear FRF. In [11], the nonlinear normal modes of a shell-like structure are sought by applying the restoring force surface method, however gaining conspicuous modelling errors. All the methods presented in [9–11] work in the modal domain. Also, they rely on not so powerful nonlinear system identification algorithms, which may struggle in the case of multiple modes interactions.

In this paper, a novel methodology is presented to identify structures exhibiting distributed nonlinearities using experimental data under a broadband gaussian excitation. Therefore, multiple modes are excited simultaneously, and no restrictions about the possible internal interactions are made. This is accomplished by extracting the nonlinear model directly from the measurements via nonlinear system identification in the modal domain, using an appropriate algorithm. Thus, the LNMs are first extracted from the measurements and then they are used to obtain the nonlinear reduced-order model. An ad-hoc version of the nonlinear subspace identification (NSI) algorithm [12,13] working in the reduced-order domain is used, but the presented methodology can in principle be applied with other nonlinear identification tools. In its original form, NSI has proved to be a robust and powerful method for dealing with localized nonlinearities [14], and thus it seems a convenient choice for the problem presented here. The whole methodology is validated on experimental data of a very thin beam exhibiting a distributed nonlinear behavior.

2. Nonlinear system identification strategy

The purpose of this paper is to perform an experimental identification of a structure exhibiting a distributed nonlinear behavior. To do so, the measured data is first projected onto a reduced-order domain using the LNMs as projection basis. Therefore, the obtained modal model is used as the reference model for the identification algorithm. If a black-box identification method is used, the data itself is generally enough to perform the identification, as no further a priori information is required. On the other hand, if a white/gray-box identification technique is adopted, then the input-output data has to be linked to some a priori knowledge

about the dynamical behavior of the structure. This is the case of the nonlinear subspace identification (NSI) method [12,13], which requires the knowledge of the nonlinear basis functions .

Whatever algorithm is used, there are some key steps which stay the same in the nonlinear identification strategy. In particular, the LNMs are needed in order to build the reduced-order domain. It is important to highlight that the LNMs have to be computed just in the points where the sensors are located. In other words, a full analytical description of the mode shapes is not needed. This implies that a low-excitation level test should be performed first to extract the modal parameters using a linear identification algorithm. The nonlinear identification strategy is summarized in Figure 1.

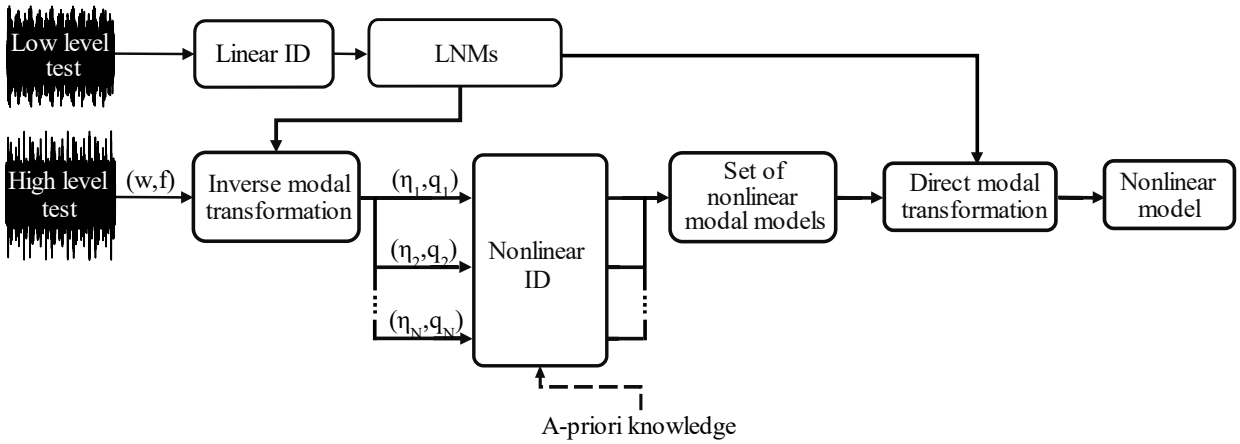

Figure 1: Flowchart of the nonlinear system identification strategy.

NSI is used in the following to identify the nonlinear model and a brief description of the method is here reported.

2.1. **Nonlinear subspace identification (NSI) in the modal domain**

NSI is a gray-box identification tool able to perform the nonlinear system identification of vibrating mechanical structures. It was developed in both time and frequency domains with the names of TNSI [12] and FNSI [13], respectively. The two methods share the same background and differ in the domain in which they operate, each one having advantages and disadvantages depending on the specific situation [14]. In this paper, the authors will generally refer to NSI to address the family of methods, unless specified otherwise. The NSI method relies on the feedback interpretation of nonlinear mechanical systems [15], treating the nonlinear restoring force as

a feedback to the underlying linear system. Considering a generic continuous nonlinear system, this is equivalent to writing:

$$M\left[\frac{\partial^2}{\partial t^2}\mathrm{w}(\mathbf{x},t)\right]+C_v\left[\frac{\partial}{\partial t}\mathrm{w}(\mathbf{x},t)\right]+K[\mathrm{w}(\mathbf{x},t)]=\mathrm{f}(\mathbf{x},t)-\mathrm{f}^{\mathrm{nl}}(\mathrm{w},\dot{\mathrm{w}}),\quad \mathbf{x}\in\mathcal{D} \tag{1}$$

where $\mathrm{w}(\mathbf{x},t)$ is the displacement of the spatial coordinate $\mathbf{x}$ in the domain $\mathcal{D}$; M and K are the mass and stiffness linear differential operators [16], C_v is the proportional viscous damping operator, and $\mathrm{f}(\mathbf{x},t)$ is the forcing input. The term $\mathrm{f}^{\mathrm{nl}}(\mathrm{w},\dot{\mathrm{w}})$ represents the nonlinear restoring force, i.e. the nonlinear part of the equation. It is put into the right-hand side so that it becomes a feedback to the underlying linear system on the left-hand side and it is generally a function of both displacements w and velocities $\dot{\mathrm{w}}$. For the case studied here, a distributed nonlinear behavior is considered and the LNMs ϕ are used to operate in the modal domain. Using the expansion theorem, the solution of eq. (1) can be expressed as:

$$\mathrm{w}(\mathbf{x},t)\cong\sum_{\mathrm{j}=1}^{\mathrm{N}}\phi_{\mathrm{j}}(\mathbf{x})\eta_{\mathrm{j}}(t) \tag{2}$$

where $\eta_{\mathrm{j}}(\mathrm{t})$ is the j^{th} modal coordinate and a total of N LNMs are taken into account. This choice is very common when dealing with distributed nonlinearities due to its simplicity. However, it should be highlighted that LNMs do not decouple the equations of motion in a nonlinear setting. A good accuracy is preserved for moderately-large amplitude vibrations and when large rotations are not present [17]. This idea is deepened in sections 3 and 4, where the application of this methodology to a nonlinear beam showing axial-bending coupling is considered. Applying the modal transformation expressed by eq. (2) to eq. (1) and under the assumption of self-adjoint operators, the following set of equations can be obtained:

$$\mathrm{m_r}\ddot{\eta}_{\mathrm{r}}+\mathrm{c_r}\dot{\eta}_{\mathrm{r}}+\mathrm{k_r}\eta_{\mathrm{r}}=\mathrm{q_r}-\mathrm{q_r^{nl}},\quad \mathrm{r}=1,2,\dots,\mathrm{N} \tag{3}$$

where $\mathrm{m_r}$, $\mathrm{c_r}$ and $\mathrm{k_r}$ are the modal mass, damping and stiffness respectively, and $\mathrm{q_r}(t)=\int_{\mathcal{D}}\phi_{\mathrm{r}}(\mathbf{x})\mathrm{f}(\mathbf{x},t)d\mathcal{D}$ is the modal force. The nonlinearity is now expressed by the term $\mathrm{q_r^{nl}}(t)=\int_{\mathcal{D}}\phi_{\mathrm{r}}(\mathbf{x})\mathrm{f}^{\mathrm{nl}}(\phi,\eta,\dot{\eta})d\mathcal{D}$. It is assumed hereafter that this term can be written as a linear-in-the-parameters basis function expansion up to a certain number J:

$$\mathrm{q_r^{nl}}=\sum_{\mathrm{j}=1}^{\mathrm{J}}\mathrm{q_{j,r}^{nl}}=\sum_{\mathrm{j}=1}^{\mathrm{J}}\Gamma_{\mathrm{j,r}}\,\mathrm{b_{j,r}} \tag{4}$$

Each contribution $q_{j,r}^{nl}$ contains an unknown coefficient $\Gamma_{j,r}$ and a nonlinear basis function $b_{j,r}$ that is supposed to be known. The expression of $b_{j,r}$ for the practical application examined in this work is derived in section 3. Eq. (3) can be seen as a system having J nonlinearities for each mode r, which are treated as feedbacks to the underlying linear modal model. The extended modal input vector $\mathbf{q}_r^e(t)$ can be defined as:

$$\mathbf{q}_r^e(t) = \begin{bmatrix} q_r(t) & b_{1,r}(t) & \dots & b_{J,r}(t) \end{bmatrix}^T \tag{5}$$

The subscript *r* is omitted hereafter to ease the notation, stating that all the steps refer to a single mode. If a state vector $\boldsymbol{\lambda} = [\eta \quad \dot{\eta}]^T$ is defined, a nonlinear discrete time state-space formulation can be retrieved:

$$\begin{cases} \boldsymbol{\lambda}(\tau+1) = \mathbf{A}\boldsymbol{\lambda}(\tau) + \mathbf{B}^e\mathbf{q}^e(\tau) \\ \eta(\tau) = \mathbf{C}\boldsymbol{\lambda}(\tau) + \mathbf{D}^e\mathbf{q}^e(\tau) \end{cases} \tag{6}$$

where τ is the sampled time and the superscript *e* stands for *extended*. The matrices $\mathbf{A}, \mathbf{B}^e, \mathbf{C}, \mathbf{D}^e$ are the state, extended input, output and extended direct feedthrough matrices, respectively. It follows from eq. (6) that recasting the nonlinear feedbacks into the extended modal input vector results in a multi-input system, with $J + 1$ forcing functions. Also, eq. (6) represents in principle a single-degree-of-freedom system in the case of linear systems, as it is the result of the modal transformation. The model order in the state-space formulation is then theoretically equal to two. Therefore, the abovementioned matrices can be written as follows, assuming that displacements are measured:

$$\mathbf{A} = \begin{bmatrix} 0 & 1 \\ -m_r^{-1}k_r & -m_r^{-1}c_r \end{bmatrix} \in \mathbb{R}^{2\times2}, \quad \mathbf{B}^e = \begin{bmatrix} 0 & 0 & \dots & 0 \\ m_r^{-1} & m_r^{-1}\Gamma_{1,r} & \dots & m_r^{-1}\Gamma_{J,r} \end{bmatrix} \in \mathbb{R}^{2\times(J+1)}$$
$$\mathbf{C} = [1 \quad 0] \in \mathbb{R}^{1\times2}, \quad \mathbf{D}^e = [0 \quad 0 \quad \dots \quad 0] \in \mathbb{R}^{1\times(J+1)} \tag{7}$$

Subspace identification can be performed to identify the state-space matrices, rearranging the measured displacements into Hankel-type block matrices. The idea is borrowed from the linear subspace identification theory (SI) [18,19], and detailed steps in the nonlinear case can be found in [12]. If the identification is performed in the frequency domain (FNSI), the discrete Fourier transform is first applied to eq. (6). A detailed formulation of FNSI is reported in [13].

For nonlinear systems, the LNMs can be used as a reduction basis in a Galerkin sense, but they do not guarantee a full decoupling. In the following, no assumption is made about the order of the modal model and stabilization diagrams will be used in the practical application to select the best model order on a case-by-case basis [14].

Once a state-space model $\mathbf{A}, \mathbf{B}^{\mathrm{e}}, \mathbf{C}, \mathbf{D}^{\mathrm{e}}$ is identified, the final step is the estimation of the nonlinear coefficients Γ_{j} and of the FRF of the underlying linear (and modal) system $\mathrm{H}(\omega)$. In particular, the extended FRF matrix $\mathbf{H}^{\mathrm{e}}(\omega)$ can be obtained from:

$$\mathbf{H}^{\mathrm{e}}(\omega) = \mathbf{D}^{\mathrm{e}} + \mathbf{C}(\mathrm{z}\mathbf{I} - \mathbf{A})^{-1}\mathbf{B}^{\mathrm{e}}, \quad \mathrm{z} = \mathrm{e}^{i\omega\Delta\mathrm{t}} \tag{8}$$

where $\mathbf{I}$ is the identity matrix and i is the imaginary unit. $\mathbf{H}^{\mathrm{e}}(\omega)$ has the same structure as the extended force vector $\mathbf{q}^{\mathrm{e}}$:

$$\mathbf{H}^{\mathrm{e}}(\omega) = \left[\mathrm{H}(\omega), \quad \Gamma_1^{\mathrm{id}}\mathrm{H}(\omega), \quad \dots, \quad \Gamma_{\mathrm{j}}^{\mathrm{id}}\mathrm{H}(\omega)\right] \tag{9}$$

so that its first block $\mathrm{H}(\omega)$ is the FRF of the underlying linear (and modal) system. The nonlinear coefficients $\Gamma_{\mathrm{j}}^{\mathrm{id}}$ can eventually be deduced from the remaining blocks [12]. Note that this operation results in frequency-dependent and complex-valued coefficients. Since the coefficients Γ_{j} are real quantities, the ratio between the real part of $\Gamma_{\mathrm{j}}^{\mathrm{id}}$ and its imaginary part is a meaningful tool to assess the quality of the identification outcome, as the imaginary part should be zero in absence of noise and of modeling errors [12].

If the steps described in eqs. (3)-(9) are repeated for each participating mode *r*, a set of N nonlinear modal state-space models $\{\mathbf{A}, \mathbf{B}^{\mathrm{e}}, \mathbf{C}, \mathbf{D}^{\mathrm{e}}\}_{\mathrm{r}}$ is obtained together with the full matrix of coefficients $\mathbf{\Gamma}^{\mathrm{id}}$.

A further improvement of the method can be obtained by minimizing the errors over the residuals of the outputs [20]. First, the outputs in the modal domain η^{id} are generated using the identified state-space model and the measured (modal) input. Then, the difference between those and the measured modal outputs η is minimized in a least-square sense tuning the identified state-space matrices. This minimization can be carried out either in time or frequency domain. The latter also allows to choose a weighting function so as to give more importance to particular frequency ranges. For instance, the minimization problem in the time domain can be written as:

$$\hat{\theta} = \arg\min_{\theta} \sum_{\tau} \left|\eta(\tau) - \eta^{\mathrm{id}}(\tau)\right|^2 \tag{10}$$

where $\theta = \mathrm{vec}([\mathbf{A} \quad \mathbf{B}^{\mathrm{e}} \quad \mathbf{C} \quad \mathbf{D}^{\mathrm{e}}])$ and the vector operation $\mathrm{vec}(\cdot)$ stacks the column of a matrix on top of each other. The physical nonlinear model can eventually be assembled by computing the direct modal transformation, as in Figure 1. Thus, the simulated physical outputs w^{id} can be computed from eq. (2) when the modal outputs η^{id} are considered. The FRF of the physical underlying linear system, called $\mathrm{G}(\omega)$, can be

computed similarly by summing the contributions of the considered modes expressed by the modal FRFs $\mathrm{H_r}(\omega)$ of eq. (9), with $\mathrm{r} = 1, \dots, \mathrm{N}$, and knowing the corresponding LNMs.

3. Geometrically nonlinear beam: a modal model

A slender beam undergoing large flexural vibrations is considered. The governing equation is reported in eq. (11) [1]:

$$\mu \frac{\partial^2 \mathrm{w}}{\partial t^2} + \mathrm{c}_v \frac{\partial \mathrm{w}}{\partial t} + \mathrm{EI} \frac{\partial^4 \mathrm{w}}{\partial x^4} - \mathrm{EA} \left(\frac{\partial \mathrm{u}}{\partial x} + \frac{1}{2} \left(\frac{\partial \mathrm{w}}{\partial x} \right)^2 \right) \frac{\partial^2 \mathrm{w}}{\partial x^2} = \mathrm{f}(t)\, \delta(x - x_\mathrm{f}) \tag{11}$$

where $\mathrm{w}(x,t)$ is the flexural displacement, $\mathrm{u}(x,t)$ is the axial displacement, μ is the linear density (kg/m), c_v is the viscous damping parameter (Ns/m), E is the Young's modulus (Pa), I is the moment of inertia (m^4), A is the transversal section of the beam (m^2), $\mathrm{f}(t)$ is the external punctual force (N) applied at position x_f and δ is the Dirac's delta. It should be noted that eq. (11) has the same form of eq. (1), where the linear operators and the nonlinear function are made explicit according to the considered case and the spatial coordinate x has one dimension.

This equation is originally derived neglecting inertial and curvature nonlinear terms thanks to the slenderness assumption. Also, a proportional viscous damping is considered to account for dissipation. When the flexural deflection is large, the axial force plays a significant role in carrying transverse loads, and geometrical nonlinearities couple the equations governing the extension and bending vibrations [21]. This phenomenon is expressed in eq. (11) by the nonlinear term, which depends on a varying tensile force T(*x*,*t*) acting on the beam:

$$\mathrm{T}(x,t) = \mathrm{EA} \left(\frac{\partial \mathrm{u}}{\partial x} + \frac{1}{2} \left(\frac{\partial \mathrm{w}}{\partial x} \right)^2 \right) \tag{12}$$

If the beam has fixed edges, i.e. it is simply supported or clamped, the nonlinear term produces a stretching effect and eq. (11) can be written as [1, pp. 224-225]:

$$\mu \frac{\partial^2 \mathrm{w}}{\partial t^2} + \mathrm{c}_v \frac{\partial \mathrm{w}}{\partial t} + \mathrm{EI} \frac{\partial^4 \mathrm{w}}{\partial x^4} - \frac{\mathrm{EA}}{2\mathrm{l}} \left(\int_0^{\mathrm{l}} \left(\frac{\partial \mathrm{w}}{\partial x} \right)^2 dx \right) \frac{\partial^2 \mathrm{w}}{\partial x^2} = \mathrm{f}(t)\, \delta(x - x_\mathrm{f}) \tag{13}$$

where l is the length of the beam (m). Note that a similar expression can also be obtained in the case of non-ideal boundary conditions, which is the case of realistic non-perfect clamps [9]. Solutions to eq. (13) can be found projecting the physical domain onto a convenient reduced-order basis. If linear normal modes $\phi(x)$ are

chosen as projection space, this operation is simply the modal transformation expressed in eq. (2). Eq. (13) can then be multiplied by a generic eigenfunction $\phi_r(x)$ and integrated over the spatial domain, yielding:

$$\mu \int_l \left(\phi_r \sum_j \phi_j \ddot{\eta}_j\right) dx + c_v \int_l \left(\phi_r \sum_j \phi_j \dot{\eta}_j\right) dx + EI \int_l \left(\phi_r \sum_j \phi_j^{IV} \eta_j\right) dx - \frac{EA}{2l} \int_l \phi_r \left[\int_l \left(\sum_j \phi_j^I \eta_j\right)^2 dx \cdot \sum_j \phi_j^{II} \eta_j\right] dx = q_r(t) \tag{14}$$

In general, the integral $\int_l \left(\sum_j \phi_j^I \eta_j\right)^2 dx$ contains all the terms of the summation:

$$\int_l \left(\sum_{j=1}^{J} \phi_j^I \eta_j\right)^2 dx = \int_l \left(\sum_{k=1}^{J} \phi_k^I \eta_k\right)\left(\sum_{m=1}^{J} \phi_m^I \eta_m\right) dx \tag{15}$$

As in eq. (4), the number of nonlinear couplings is defined by the index J. Note that J is a user-defined quantity and it cannot exceed N, when N modes are taken into the solution. It is assumed in the following that the off-diagonal terms of the summation (i.e. the integrals $\int_l \phi_k^I \phi_m^I \, dx$, with $k \neq m$) can be neglected. This is true, for instance, for the simply-supported case [22]. In the case of more complex boundary conditions, the off-diagonal contributions might be non-zeros, and they should be included in the description of the nonlinearity as well. A practical example of how this can be done in the identification process will be given in section 5.2.2. Eq. (14) can therefore be written as:

$$m_r \ddot{\eta}_r + c_r \dot{\eta}_r + k_r \eta_r - \frac{EA}{2l} \sum_{j=1}^{J} \left(\alpha_j \eta_j^2\right) \beta_r \eta_r = q_r, \quad r = 1, 2, \dots, N \tag{16}$$

where the notation is the same of eq. (3), and the coefficients α_j and β_r are equal to:

$$\alpha_j = \int_l \phi_j^{I^2} dx, \quad \beta_r = \int_l \phi_r \phi_r^{II} dx \tag{17}$$

Equivalent formulations to eq. (16) can be found in [5,9,22]. The nonlinear coefficients α_j and β_r depend only on the geometrical properties of the beam and the boundary conditions, and they can be recast into a matrix $\boldsymbol{\Gamma}$:

$$\boldsymbol{\Gamma} = \frac{EA}{2l} \begin{bmatrix} \alpha_1\beta_1 & \cdots & \alpha_1\beta_N \\ \vdots & \ddots & \vdots \\ \alpha_J\beta_1 & \cdots & \alpha_J\beta_N \end{bmatrix} \in \mathbb{R}^{J \times N} \tag{18}$$

Thus, eq. (16) can be written as:

$$m_r\ddot{\eta}_r + c_r\dot{\eta}_r + k_r\eta_r - \sum_{j=1}^{J}(\Gamma_{j,r}\eta_j^2)\eta_r = q_r, \quad r = 1, 2, \dots, N \tag{19}$$

The model described by eq. (19) is validated numerically in the following section. The nonlinear part of eq. (19) is then used as an a priori information for the experimental identification of a nonlinear beam conducted with NSI (section 5).

3.1. **Numerical validation**

The proposed model, expressed by eq. (19), is validated numerically by comparing its outcome with a geometrically exact FE model based on a local frame approach [23]. A clamped-clamped beam having the properties reported in Table 1 is considered. The beam is excited with a frequency sweep over the first mode considering two different amplitudes. The lowest excitation level can be considered as linear, with an amplitude of 0.01 N. Instead, the higher excitation level is noticeably nonlinear, with an amplitude of 0.1 N. The corresponding natural frequency is 20.75 Hz, and the sweep goes from 16 Hz to 28 Hz with a rate of 0.1 Hz/s. As for the discretization, 40 nodes are considered for the FE model and a sampling frequency of 5000 Hz is used. It should be noted that the number of nodes is not defined in the proposed approach, as it is a continuous model relying on a mode superposition approach. On the other hand, the number of modes retained is a crucial parameter. In this case, N=J=3 modes are included.

Table 1: Properties of the numerical beam

Length (mm)	Width (mm)	Thickness (mm)	Young's Modulus (MPa)	Density (kg/m^3)	Viscous damping (Ns/m)
500	20	1	200	7800	0.47

The values of the coefficients $\Gamma_{j,r}$ computed analytically using eq. (18) are reported in Figure 2. The off-diagonal terms are neglected in the considered model, as just the first mode is excited. The matrix $\boldsymbol{\Gamma}$ is symmetric in the case of fixed edges, and the magnitudes of its entries increase together with the considered mode.

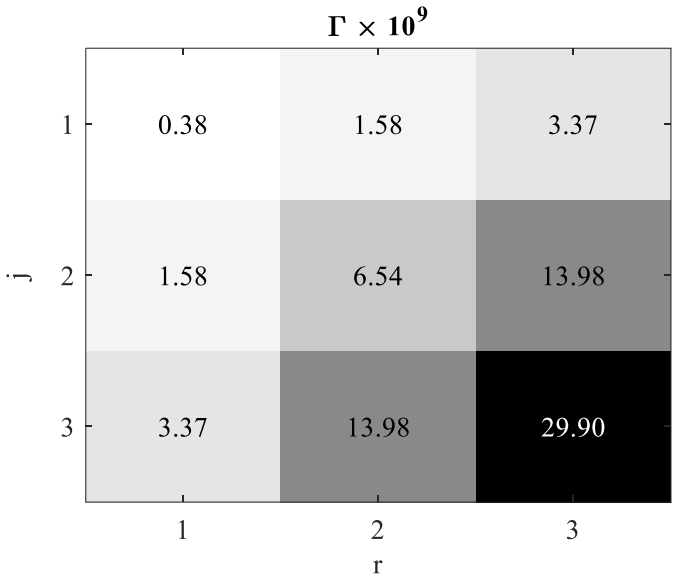

Figure 2: Analytical coefficients $\Gamma_{j,r}$ of the numerical beam. The background color of each entry is proportional to its magnitude.

The excitation is applied at 5 cm from one end, and the response is computed at the mid-span node. Time integration is performed with the Generalized-α method [24] for both approaches with no numerical damping ($\alpha_m = \alpha_f = 0, \gamma = 1/2\,, \beta = 1/4$). The outcome of the proposed approach and of the FE model are reported in Figure 3.

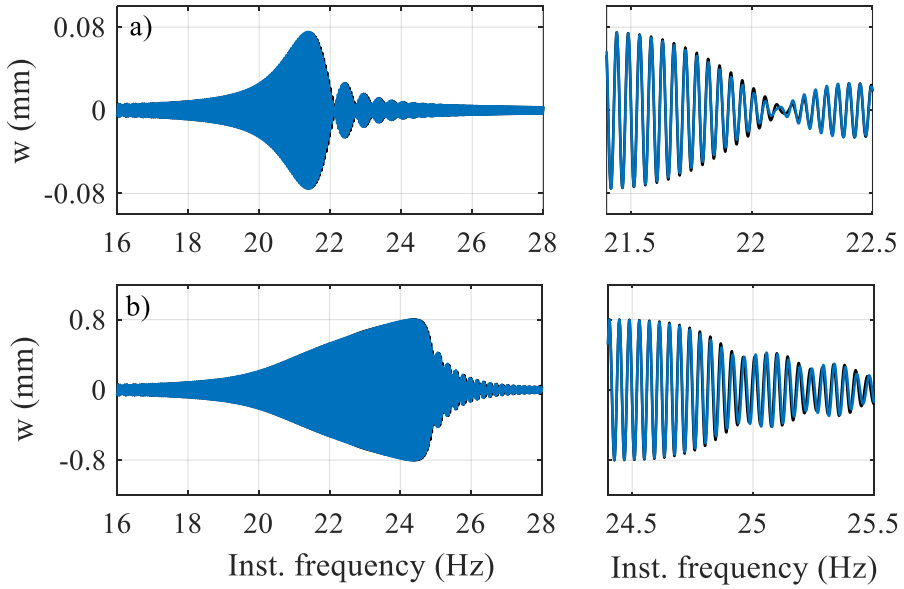

Figure 3: Time response of the numerical beam with different excitation levels. Black line: proposed approach; blue line: FEM. a) linear excitation level with zoom around the resonance peak; b) nonlinear excitation level with zoom around the jumping frequency.

The response computed with the mode superposition approach well matches the one computed with the local frames FEM for the lowest excitation level. There is still a minor difference in Figure 3a around the resonance

peak, which is allegedly due to the different beam models used by the two approaches. While the mode superposition method is based on the Euler-Bernoulli formulation, the local frames FE method is based on the Timoshenko formulation. The two formulations are indeed very similar for slender beams like the one considered here, but there is still a slight difference in the computation of the natural frequency, which is approximately 20.82 Hz for the local frame FEM against 20.75 Hz for the proposed approach, leading to a small phase shift (~ 0.3%). As for the nonlinear level in Figure 3b, a characteristic hardening effect coming from the stretching of the neutral axis is visible and the two methods well agree, though some difference is present around the jumping frequency for the same reasons as before. The maximum frequency shift between the two responses is in this case approximately 0.2%, while the percentage RMS difference in amplitude is around 3%.

4. The experimental setup

The experimental setup involves a clamped-clamped slender beam instrumented with accelerometers and excited with a shaker. A sketch of the test rig is reported in Figure 4.

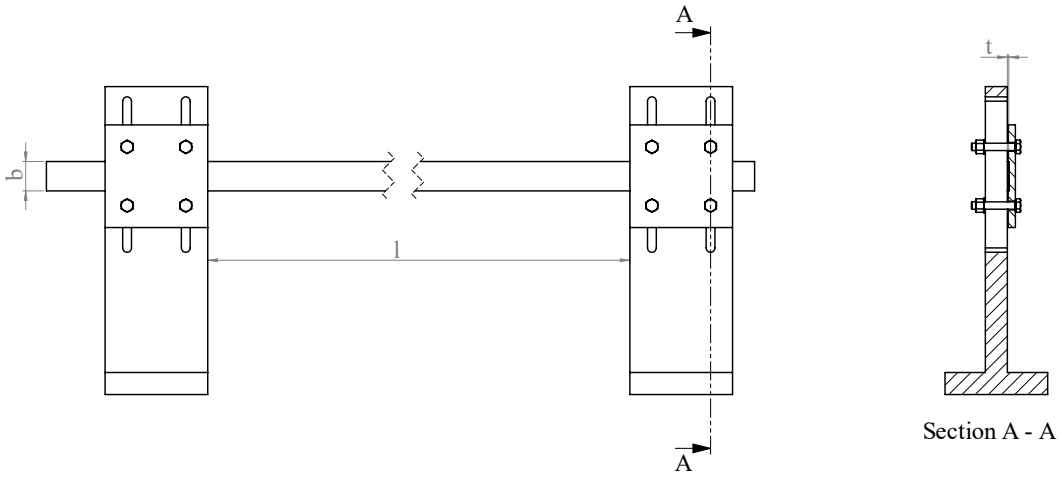

Figure 4: Sketch of the experimental test rig.

The properties of the beam are reported in Table 2, while a picture of the experimental setup can be seen in Figure 5.

Table 2: Properties of the experimental beam

Length (mm)	Width (mm)	Thickness (mm)	Material
479	20	0.75	Carbon steel

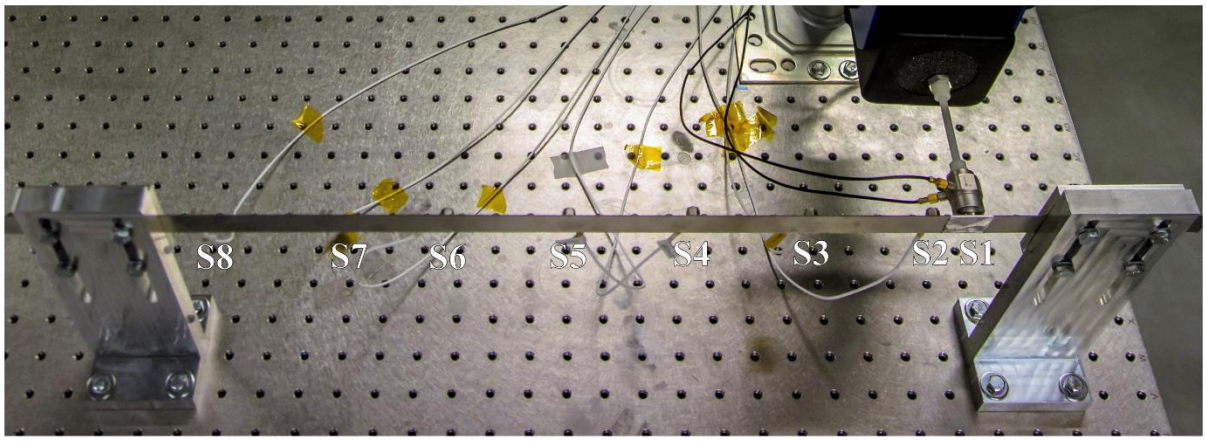

Figure 5: Photo of the experimental test rig.

A total of 8 accelerometers are used, plus a load cell on the head of the shaker to record the input. The position of the sensors is summarized in Table 3.

Table 3: Position of the sensors along the length of the beam and type.

Sensor #	Distance from the right end (mm)	Type	Name	Weight (g)
S1	15	Impedance head	Dytran 5860B	60
S2	35			
S3	105			
S4	175			
S5	245	Accelerometer	Dytran 3035B2	2.5
S6	315			
S7	385			
S8	455			

The beam is excited with a random phase multisine input [25] encompassing the first three bending modes. The chosen frequency range is from 14 Hz to 100 Hz. The sampling frequency is $f_s = 6400$ Hz, and a total of $M = 5$ realizations with $P = 6$ periods and $N_s = 65536$ spectral lines per period are considered. The different periods and realizations are used in the following section to characterize the nonlinearity. Several forcing levels are considered, ranging from a linear behavior ($f_0 = 0.2$ N RMS) to a highly nonlinear one ($f_0 = 3$ N RMS).

4.1. **Characterization of the nonlinearity**

Figure 6a represents the acceleration of the fifth sensor over the first realization for different forcing levels in the time domain. The corresponding experimental FRF is depicted in Figure 6b together with the coherence function γ^2. As expected, a distinctive hardening effect can be seen in Figure 6b on the excited modes when moving from low to high excitation levels, together with a decrease of the coherence, especially around the resonance regions.

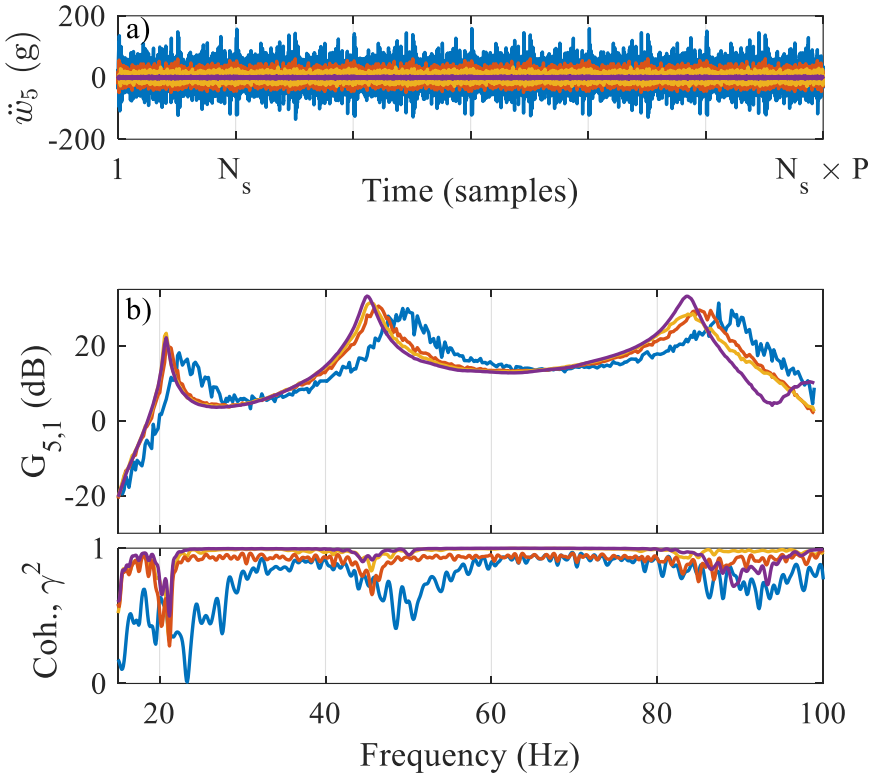

Figure 6: First realization output of sensor 5 and corresponding FRFs for different forcing levels f_0. Purple line: $f_0 = 0.2$ N; Yellow line: $f_0 = 1$ N; Red line: $f_0 = 1.7$ N; Blue line: $f_0 = 3$ N. a) Time domain; b) Experimental FRF (inertance) in dB scales (ref. 1 g^2/N) and coherence plot.

Moreover, as a random-phase multisine is a periodic signal, the periodicity of the output can be investigated as well. By analyzing the variations of the periodic input and output signals over the measurements of the repeated periods, the sample mean and the sample covariance of the input and the output disturbing noise can be calculated, as a function of the frequency. Although the disturbing noise varies from one period to the other, the nonlinear distortions do not [26]. This means that noise and nonlinear distortions can be separated to actually check how the nonlinear system behaves. Also, the amount of even and odd nonlinearities can be detected by carefully choosing the excited frequency lines. If the input spectrum contains only odd frequency lines and some of them are randomly missing, then these should not be present in the output if the system is linear. This kind of multisine is generally called odd-random multisine. When the system behaves nonlinearly, even nonlinearities (if any) show up at the even frequencies because an even number of odd frequencies is added together. Odd nonlinearities are present only at the odd frequencies because an odd number of odd frequencies is added together. At the odd frequencies that are not excited at the input, the odd nonlinear

distortions become visible at the output because the linear part of the model does not contribute to the output at these frequencies [26].

The measured output in the frequency domain is reported in Figure 7 for several odd-random multisine levels. The spectra of the disturbing noise and of the odd and even nonlinearities are also shown. It can be seen that the levels of noise and nonlinearities are similar for the lowest forcing level (Figure 7a), while their difference becomes more important as the forcing level increases. In particular, the level of the nonlinearities for the two highest inputs is very high when compared to the total output (Figure 7c,d).

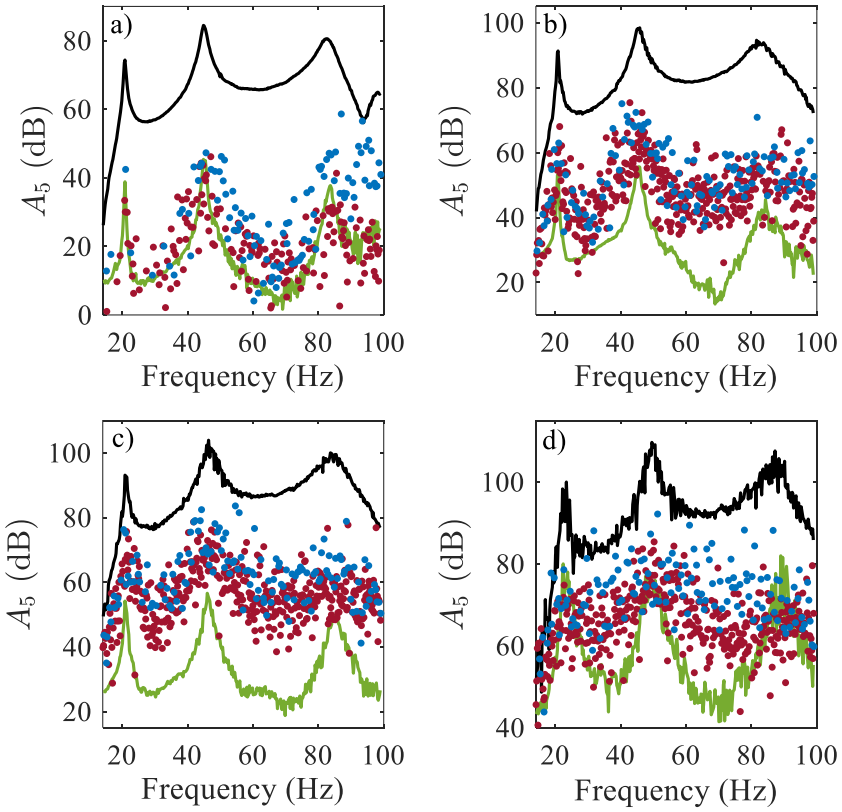

Figure 7: Odd-random multisine output for different forcing levels in dB scales (ref. 1 g^2/Hz). Black line: Output spectrum; green line: disturbance noise level; blue dots: odd nonlinearities; red dots: even nonlinearities. a) $f_0 = 0.2$ N; b) $f_0 = 1$ N; c) $f_0 = 1.7$ N; d) $f_0 = 3$ N.

This is clearer in Figure 8, showing the total distortions of the outputs for the two highest levels. It can be seen that the amount of the total distortions is very high, comparable to the level of the output in the resonance regions.

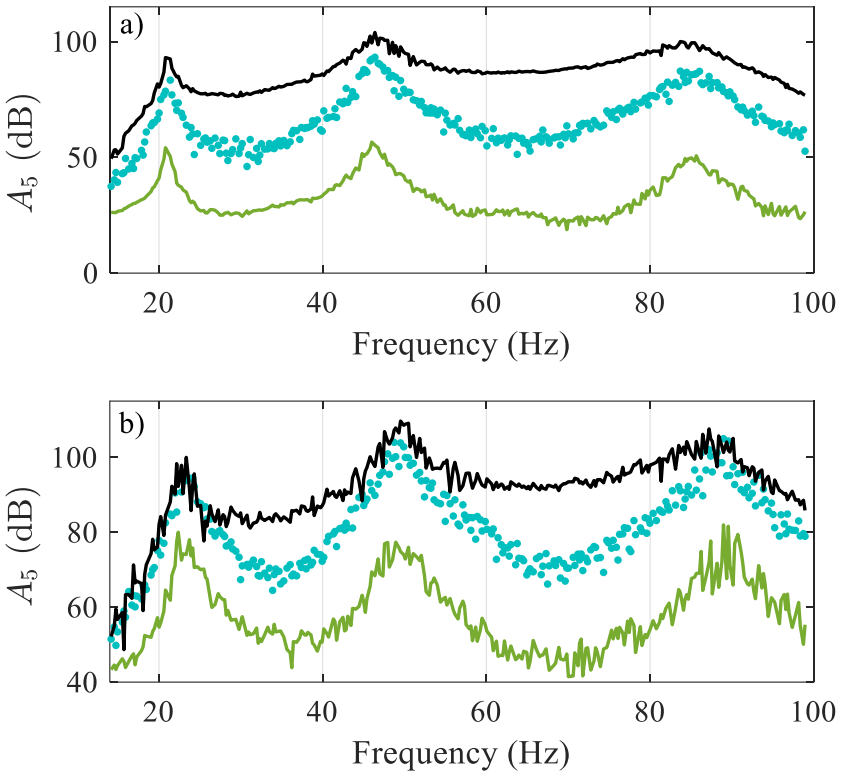

Figure 8: Odd-random multisine output for different forcing levels in dB scales (ref. 1 g^2/Hz). Black line: Output spectrum; green line: disturbance noise level; light blue dots: total distortions level. a) $f_0 = 1.7$ N; b) $f_0 = 3$ N.

Also, it is clear from Figure 7 that both odd and even nonlinearities are present for all the different levels, though odd nonlinearities seem to be slightly more important. This result is not expected from the adopted model (eq. (19)), which has no even features. That is because, generally, even nonlinearities are associated with some asymmetry in the response, which in principle should not appear in the case of a clamped-clamped beam. Nevertheless, there might be several sources of even behavior when the real structure is considered: imperfection of the clamps, possible non-planarity of the section of the beam along its length, the added mass of the shaker and the accelerometers on one side of the beam, nonlinear damping. It is not straightforward to investigate the effects related to each source, but even nonlinearities should be taken into account when proceeding with the system identification.

5. Results

The experimental setup described in section 4 is used to perform the nonlinear system identification. The beam is excited with a full random phase multisine ranging over the first three bending modes. The full multisine is chosen here instead of the odd-random (section 4.1) to maximize the number of spectral lines for a fixed

acquisition length. The tests are conducted using the same parameters of section 4. A low-amplitude test is first performed to extract the LNMs (as in Figure 1), followed by a high-amplitude test to exploit the full nonlinear behavior. Here, 4 realizations out of 5 are used as a training set for the identification, while the last one is used as a validation set.

5.1. **Identification of the LNMs**

A linear subspace identification (SI) technique is used to identify the LNMs of the beam. The RMS value of the input force is $f_0 = 0.2$ N, and the experimental FRF (receptance) related to the 2nd sensor is reported in Figure 9 together with the noise level and the total distortion level. Since all the sensors exhibit similar distortion levels, just one sensor is shown.

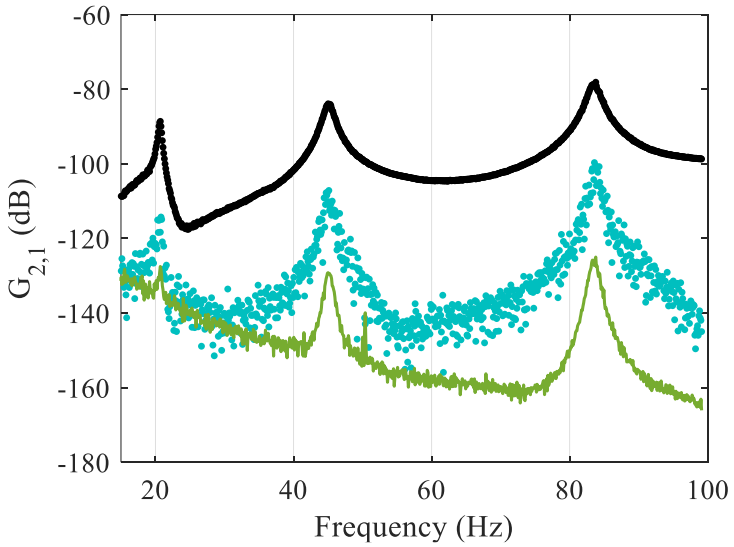

Figure 9: Experimental FRF (receptance) related to sensor 2 in dB scales (ref. 1 m/N), $f_0 = 0.2$ N (RMS). Black line: FRF; green line: disturbance noise level; light blue dots: total distortions level.

Some difference can be noted between the total distortion level and the noise level, especially around the resonance peaks. This mismatch is supposed to be caused by some source of nonlinearity, and the most likely scenario is that this is due friction between the beam and the clamps and is not related to geometrical effects. In any case, the total distortions are always at least one order of magnitude lower than the FRF. Therefore, the structure can be considered as linear at this level of excitation, and SI can be applied to extract the parameters of interest. The stabilization diagram obtained applying SI for different model orders is reported in Figure 10. Since the object of the linear identification are just the LNMs, the model order for each mode is chosen adopting a LNMs similarity criterion: all the MACs between the LNMs related to each identified mode are

compared and the model order that achieves the best MAC is selected. The modal parameters are then extracted and they are reported in Table 4.

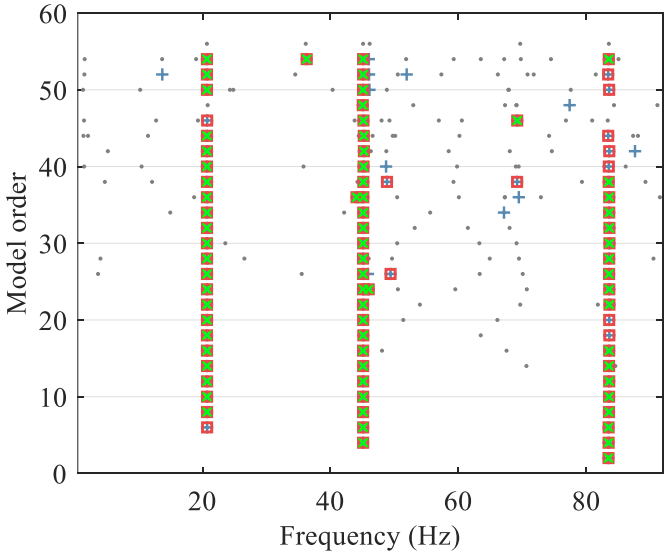

Figure 10: Stabilization diagram related to the linear subspace identification at low level. Stabilization thresholds for natural frequency, damping ratio and MAC are 0.5%, 10% and 99.5%, respectively. Gray dot: new (not stable) pole. Blue plus: pole stable in frequency. Red square: pole stable in frequency and MAC (Modal Assurance Criterion). Green cross: pole stable in frequency, MAC and damping.

Table 4: Linear modal parameters identified with SI.

Mode number	Frequency (Hz)	Damping ratio (%)
1	20.7	1.2
2	45.1	1.7
3	83.6	1.1

The deformed shapes of the first three bending modes are eventually depicted in Figure 11.

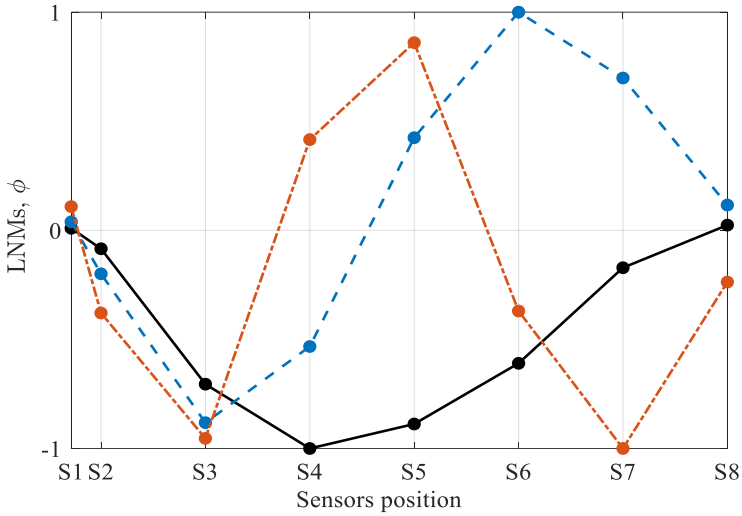

Figure 11: Experimental LNMs. Black line: first LNM; dashed blue line: second LNM; dashed-dotted red line: third LNM.

The experimental LNMs are slightly different from the theoretical ones of a clamped-clamped beam, that are symmetrical in the spatial coordinate. The reason for this difference is the attachment with the shaker in the proximity of one boundary condition, which alters the symmetry of the structure due to the added mass of the impedance head. Nevertheless, this is not an issue for the methodology, since only the experimental mode shapes are used in the nonlinear system identification.

5.2. **Nonlinear identification with NSI**

NSI is applied to the experimental setup excited with a high-amplitude input following the formulation given in section 3. The RMS value of the input force is $f_0 = 2$ N and the experimental FRF (receptance) related to the 2nd sensor is reported in Figure 12 together with the noise level and the total distortion level. Since all the sensors exhibit similar distortion levels, just one sensor is shown.

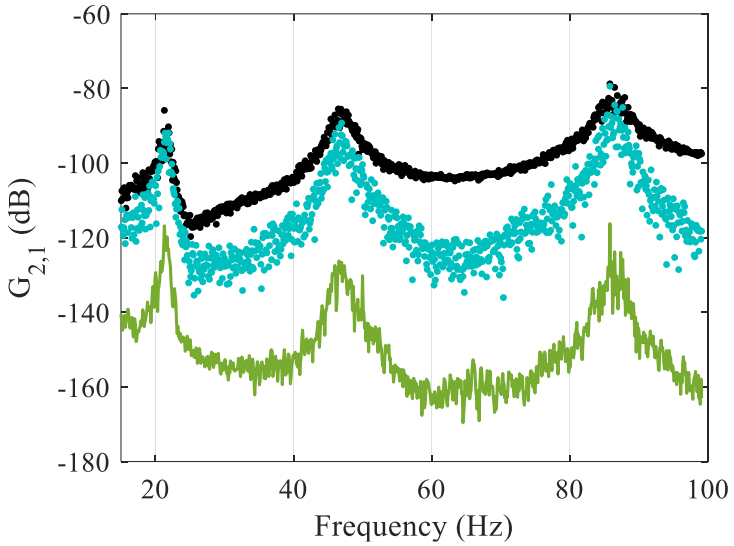

Figure 12: Experimental FRF (receptance) related to sensor 2 in dB scales (ref. 1 m/N), $f_0 = 2$ N (RMS). Black line: FRF; green line: disturbance noise level; light blue dots: total distortions level.

Here, the amount of the total distortions has almost the same level of the signal itself, especially around the resonance peaks. This ensures that the nonlinearity is properly triggered, and nonlinear system identification can be performed. In terms of shifting of the natural frequencies, all the three modes in Figure 12 show a frequency shift of approximately 5% when compared to the ones in Figure 9 (linear case).

The nonlinear basis functions $b_{j,r}$ defined in eq. (4) must be chosen in order to apply the NSI method. In particular, a first choice could be the one gathered from the modal model, eq. (19). Thus:

$$b_{j,r} = -\eta_j^2 \eta_r, \quad j = 1, \dots, J = N, \quad r = 1, \dots, N \tag{20}$$

The number of nonlinear feedbacks per mode is 3 when J=N=3. However, this nonlinear function predicts only an odd nonlinear behavior. It has been shown in section 4 that the system exhibits also a reasonable amount of even nonlinear distortions caused by some even nonlinearity. Since the nonlinear basis functions in eq. (20) are not capable of representing this kind of behavior, there will still be a part of the system response that is not captured by the identified model. Also, the off-diagonal terms of the summation of eq. (15) might give a contribution in the real case, as clamped-clamped boundary conditions are considered.

An option to overcome these issues could be to expand the basis functions so as to include all the possible couplings between any two modes (η_j, η_r) with both odd and even degrees. In this case, the nonlinear feedback of eq. (3) can be written as a sum of bivariate polynomials of maximum degree equal to 3:

$$m_r\ddot{\eta}_r + c_r\dot{\eta}_r + k_r\eta_r = q_r - q^{nl}, \quad r = 1, 2, \dots, N \tag{21}$$

where:

$$q^{nl} = \sum_{r=1}^{N}\left\{\sum_{j=1}^{J=N}\left[\sum_{m,p=1}^{2} -\Gamma^{id}_{m,p,j,r}\eta_j^m\eta_r^p\right]\right\} \tag{22}$$

The nonlinear basis functions can be recast into a vector:

$$\mathbf{b}^{nl} = -\text{vec}\{\eta_j^m\eta_r^p\} = -[\eta_1^2,\ \eta_1^3,\ \eta_1^3,\ \eta_2\eta_1,\ \eta_2^2\eta_1,\ \eta_2\eta_1^2,\ \dots,\ \eta_3^3]^T, \quad j = 1, \dots, J = N, \quad r = 1, \dots, N, \quad m = 1,2, \quad p = 1,2 \tag{23}$$

Since this vector already includes all the modes, it is possible to compute it just once and then it can be used as a feedback for each mode $r = 1, \dots, N$. The final number of nonlinear feedbacks per mode is 15 when J=N=3 and the repeated monomials are discarded.

Both options described by eq. (20) and eq. (23) are exploited in the following. The inverse modal transformation is first applied to the measured signals to compute the modal coordinates as in Figure 1. Afterwards, the nonlinear identification is performed for each mode independently.

5.2.1. **Original basis functions**

Three nonlinear feedbacks for each mode are considered as basis functions, as expressed in eq. (20). The stabilization diagram of the underlying linear system is computed for each mode in order to select the best model order and they are reported in Figure 13. Stability is checked for frequencies, damping ratios, MACs and modal masses [27]. It is clear from Figure 13 that multiple poles can be identified for each mode, as a consequence of the incomplete decoupling of the equations of motion due to the nonlinearity. The main pole for each mode generally shows full stability starting from a model order equal to 2, while the other poles tend to be unstable or stable just for high model orders. Their inclusion in the modal state-space model can lead to overfitting and an increased model sensitivity to noise, therefore 2 is selected as model order for each mode.

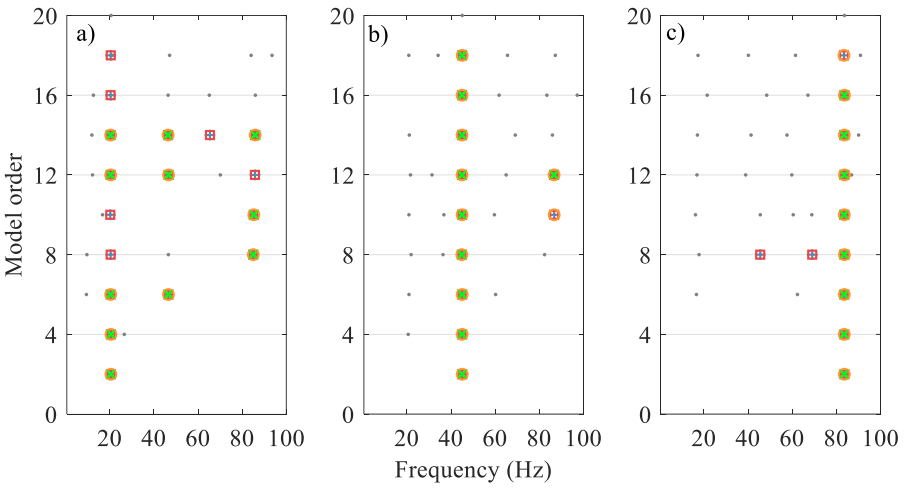

Figure 13: Stabilization diagram for NSI. Stabilization thresholds for natural frequency, damping ratio, MAC and modal mass are 0.5%, 10%, 99.5%, 10%, respectively. Gray dot: new (not stable) pole; blue plus: pole stable in frequency; red square: pole stable in frequency and MAC (Modal Assurance Criterion); orange circle: pole stable in frequency, MAC and damping; green cross: pole stable in frequency, MAC, damping and modal mass. a) Mode number 1; b) Mode number 2; c) Mode number 3.

An a posteriori optimization over the residuals of the modal outputs is carried out, as described in section 2. Once the modal state-space models have been identified, it is possible to go back to the physical domain by applying the direct modal transformation. In particular, the simulated (physical) outputs are compared with the measured ones of the validation set. The comparison is reported in the time domain in Figure 14 for the 6th sensor, the other sensors showing a similar result. In particular, the measured signal is plotted against its residual with the simulated one both before and after the final optimization. The residual appears to be relatively small, and the relative RMS error between the two signals is approximately 14% before the optimization and 10% after the optimization.

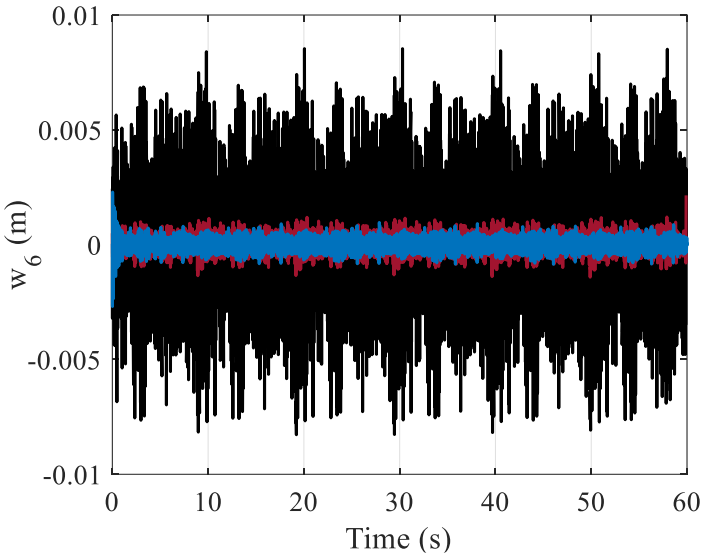

Figure 14: Validation of the nonlinear identification in the time domain. Black line: measured output, sensor 6, validation set; red line: residual with the simulated output before the optimization; blue line: residual with the simulated output after the optimization.

The same comparison can also be made in the frequency domain considering the spectra of the respective signals in the frequency range of interest. The result is depicted in Figure 15.

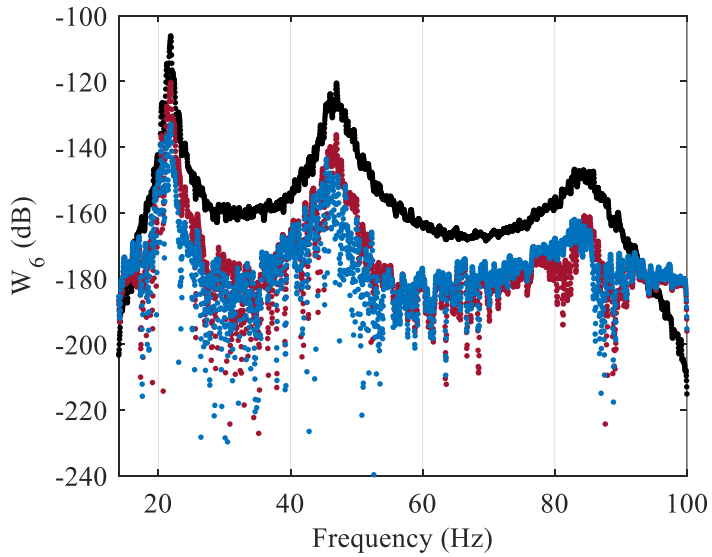

Figure 15: Validation of the nonlinear identification in the frequency domain in dB scales (ref. 1 m^2/Hz). Black line: spectrum of the measured output, sensor 6, validation set; red line: residual with the spectrum of the simulated output before the optimization; blue line: residual with the spectrum of the simulated output after the optimization.

The frequency-domain representation is particularly useful because it clearly shows the regions where the identification struggles. Before the final optimization, the region around the first natural frequency is the most

critical, with a residual 14 dB lower than the signal. The final optimization improves this result with a much smaller error. Thus, the optimized identified model is taken as the final one hereafter.

Eventually, the first three identified coefficients are reported in Figure 16 as frequency-dependent quantities in their real and imaginary parts.

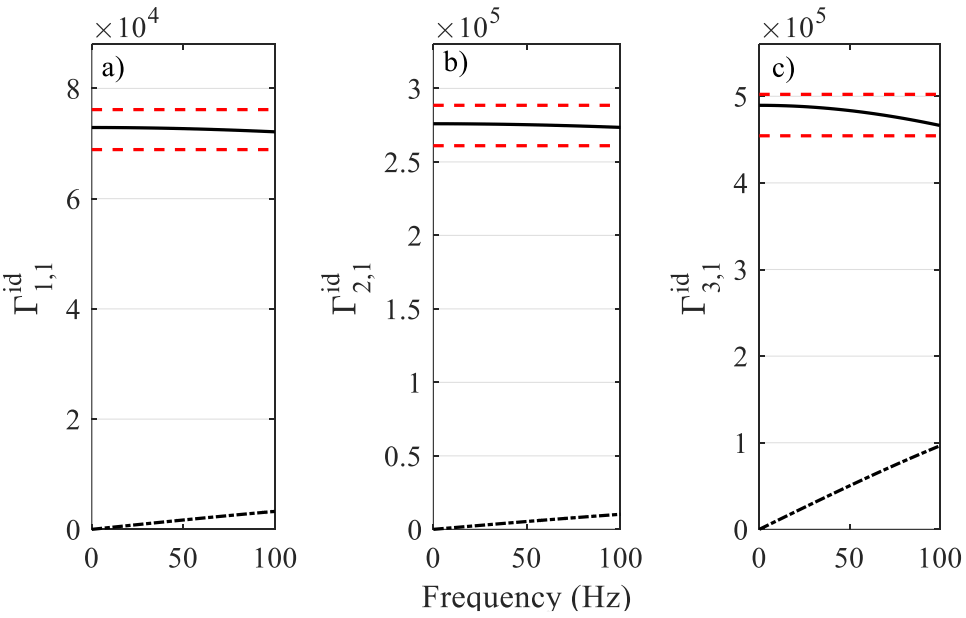

Figure 16: First three identified coefficients as frequency dependent quantities. Black continuous line: real part; black dashed-dotted line: imaginary part; red dashed line: ±5% of the mean value. a) Coefficient $\Gamma_{1,1}^{\mathrm{id}}$; b) Coefficient $\Gamma_{2,1}^{\mathrm{id}}$; c) Coefficient $\Gamma_{3,1}^{\mathrm{id}}$.

It is worth highlighting that the imaginary part is always several orders of magnitude lower than the real part, which assesses the goodness of the identification. Also, the real part shows an almost flat spectrum. Thus, the spectral mean of the real part is taken as the final value for the identified coefficients. The matrix $\boldsymbol{\Gamma}^{\mathrm{id}}$ of the identified coefficients is reported in Figure 17 together with their percentage deviation. In particular, its structure resembles the one obtained with the numerical example (section 3): the magnitudes of its entries increase together with the considered mode.

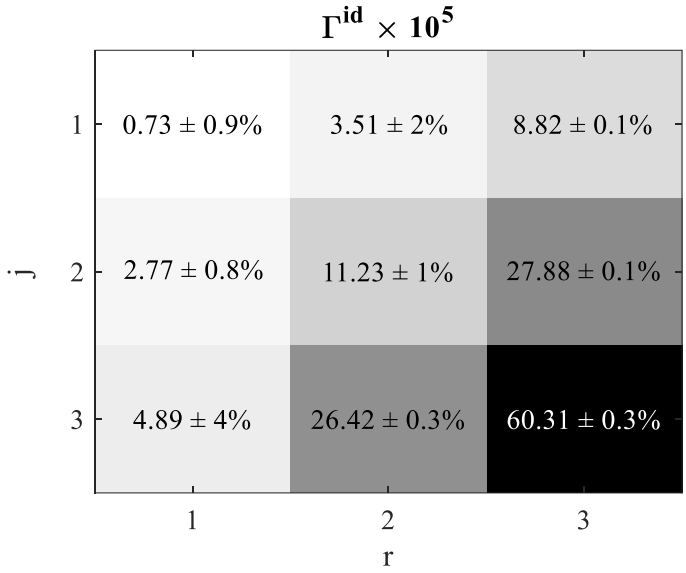

Figure 17: Identified coefficients $\Gamma_{j,r}^{id}$ of the experimental setup with their percentage deviation. The background color of each entry is proportional to its magnitude.

The underlying linear system is identified as well from eq. (8) and can be compared with the one obtained applying SI to the low-level test. The comparison is reported in Figure 18 in terms of receptance.

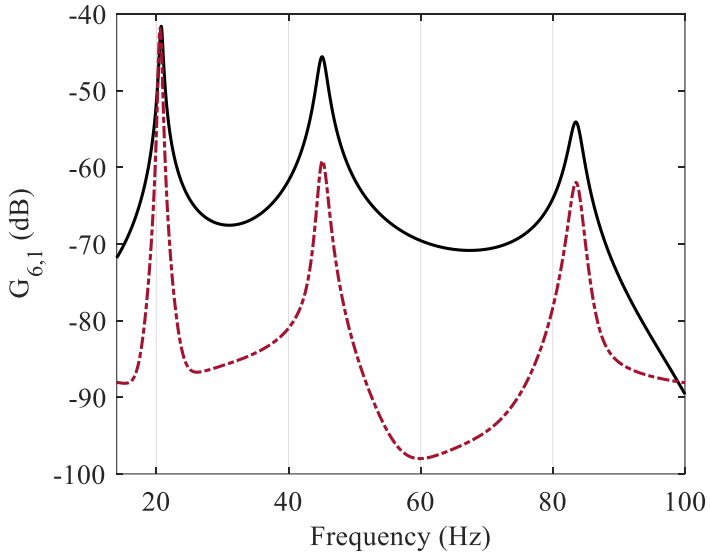

Figure 18: Estimated linear FRF (receptance) related to sensor 6 in dB scales (ref. 1 m/N). Black line: SI estimate from the low-level test; dashed-dotted red line: residual with the NSI estimate from the high-level test.

There is generally a good correspondence between the NSI estimation of the linear FRF and the SI estimation from the low-level. The highest residual corresponds to the first mode, whose identified natural frequency is slightly different for the two FRFs. The identified modal parameters are reported in the final comparison table in section 5.2.3.

5.2.2. **Extended basis functions**

When the extended basis functions in eq. (22) are considered, a total of 15 nonlinear feedbacks are present for each mode. As for section 5.2.1, the stabilization diagram of the underlying linear system is computed for each mode and the results are reported in Figure 19. The poles originating from the incomplete decoupling tend to be unstable or stable just for high model orders, while the main pole for each mode shows full stability starting from a model order equal to 2. For this reason, a model order equal to 2 for each mode is considered hereafter.

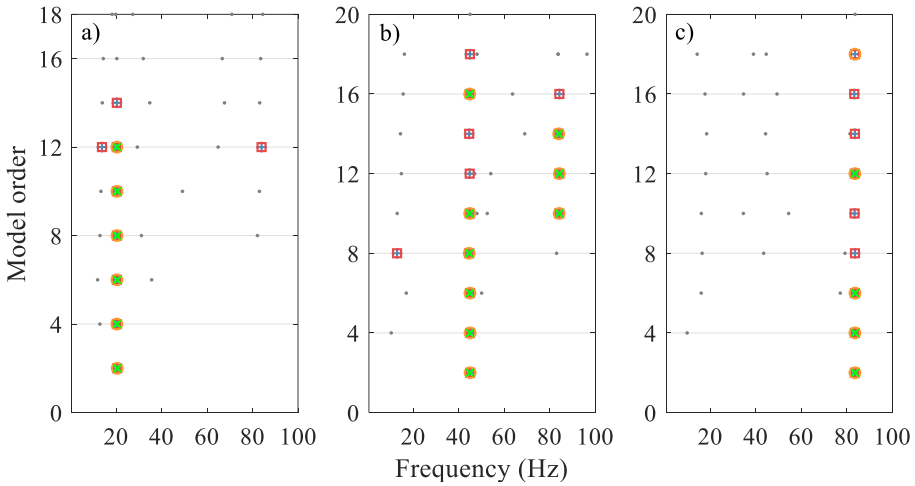

Figure 19: Stabilization diagram for NSI. Stabilization thresholds for natural frequency, damping ratio, MAC and modal mass are 0.5%, 10%, 99.5%, 10%, respectively. Gray dot: new (not stable) pole; blue plus: pole stable in frequency; red square: pole stable in frequency and MAC (Modal Assurance Criterion); orange circle: pole stable in frequency, MAC and damping; green cross: pole stable in frequency, MAC, damping and modal mass. a) Mode number 1; b) Mode number 2; c) Mode number 3.

Following the same steps of section 5.2.1, the simulated (physical) outputs are compared with the measured ones of the validation set. The comparison is reported in the frequency domain in Figure 20 for the 6th sensor. In particular, the spectrum of the measured signal is plotted against its residual with the simulated one, both before and after the final optimization. The residual now is smaller than the previous case (section 5.2.1), and the relative RMS error between the two signals in time is approximately 11% before the optimization and 6% after the optimization. The optimized identified model is taken as the final one hereafter.

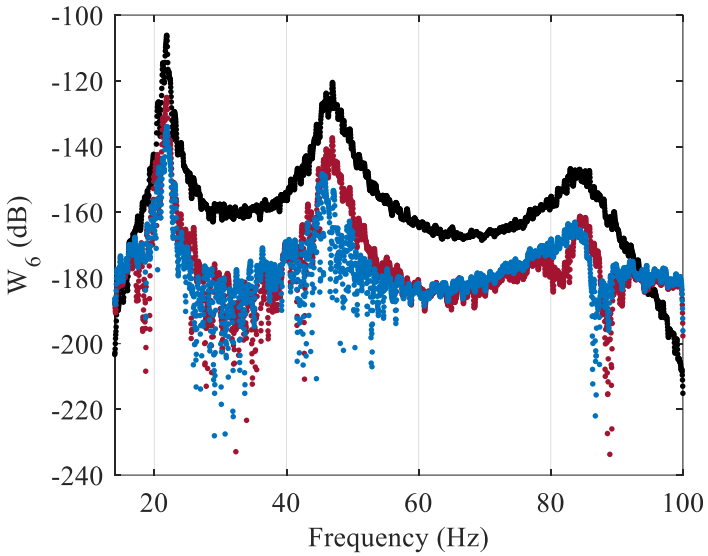

Figure 20: Validation of the nonlinear identification in the frequency domain in dB scales (ref. 1 m^2/Hz). Black line: spectrum of the measured output, sensor 6, validation set; red line: residual with the spectrum of the simulated output before the optimization; blue line: residual with the spectrum of the simulated output after the optimization.

The nonlinear coefficients are computed as well and their total number is 45. While expanding the nonlinear basis functions allows for more flexibility to catch the nonlinear part of the response, it makes the nonlinear coefficients to lose their original physical interpretation. Therefore, the representation of all the identified coefficients is not useful in this case, because no meaning can be directly associated to them. Instead, it may be informative to know which feedbacks are predominant for each identified mode. Figure 21 shows the RMS magnitude of each nonlinear feedback for the three identified modes using a gray-scale colormap. It is clear that the highest RMS on each mode corresponds to the purely cubic basis function $\eta_1^3, \eta_2^3, \eta_3^3$, respectively. Thus, the cubic nonlinearity is dominant for each mode, in accordance with the theory.

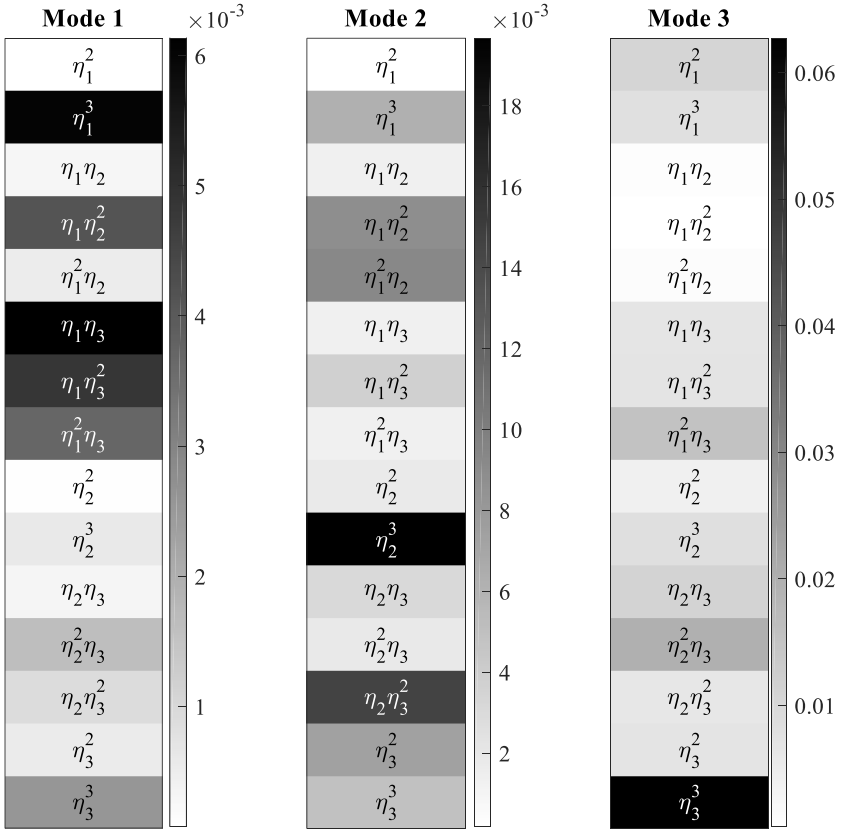

Figure 21: RMS magnitudes of the nonlinear feedbacks for the three identified modes with NSI. The background color of each entry is proportional to its magnitude.

The underlying linear system is also identified, and it is compared with the one estimated by SI. The comparison is reported in Figure 22 in terms of receptance.

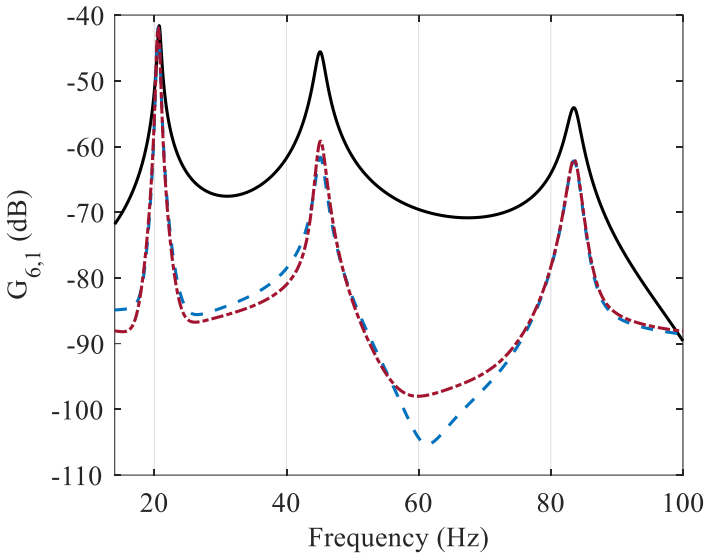

Figure 22: Estimated linear FRF (receptance) related to sensor 6 in dB scales (ref. 1 m/N). Black line: SI estimate from the low-level test; dashed-dotted red line: residual with the NSI estimate from the high-level test and the original basis functions; dotted blue line: residual with the NSI estimate from the high-level test and the extended basis functions.

Figure 22 also shows the residual between the linear FRF estimated by SI and the underlying linear FRF estimated by NSI in section 5.2.1 using the original basis functions. The residuals of the underlying linear FRF computed with NSI in the two cases (original basis functions and extended ones) seem to be comparable with each other. Therefore, it can be supposed that expanding the nonlinear basis functions in this case mostly affects the nonlinear part of the system, so that the residuals of the outputs drop from 10% to 6%. Indeed, this is generally not true, as linear parameters are affected as well by the choice of the nonlinear basis functions. In this particular case, this result confirms that the main nonlinear contributions come from the original nonlinear basis functions, and in particular from the cubic terms (Figure 21). The inclusion of the other coupling terms results just in a slight improvement of the predicted nonlinear response.

The identified modal parameters are reported in the final comparison table in section 5.2.3.

5.2.3. **Summary of the identified modal parameters**

The identified modal parameters of the underlying linear system are reported in Table 5 for the two applications of NSI and they are compared with the ones identified using SI on the linear low-level test.

Table 5: Summary of the identified modal parameters: SI, NSI with the original basis functions (Original NSI), NSI with the extended basis functions (Extended NSI).

Mode number	Frequency (Hz)			Damping ratio (%)		
	SI	Original NSI	Extended NSI	SI	Original NSI	Extended NSI
1	20.7	20.4	20.5	1.2	1.1	1.2
2	45.1	45.1	45.1	1.7	2.3	2.2
3	83.6	83.8	83.7	1.1	2.0	2.0

There is a very good correspondence in the identification of the natural frequencies, while the results related to the damping ratios are less in agreement with their corresponding low-level estimates. In particular, NSI generally identifies a higher damping than the low-level test. The reason for that may be a source of nonlinear damping that has not been considered in the model. Thus, a further improvement of the methodology should take into account also the possibility of characterizing the nonlinear damping.

As for the computational burden, NSI with the original basis functions runs in approximately 15 seconds (without the final optimization), while extending the basis functions requires 35 extra seconds on the same computer. The optimization itself requires 40 seconds for the original basis functions and 160 seconds for the extended ones.

6. Conclusions

In this paper, a methodology for performing nonlinear system identification on structures exhibiting distributed geometrical nonlinearities was presented. The system identification is performed in a reduced-order domain, obtained by first identifying the linear normal modes of the structure. An ad-hoc version of the NSI method working in the modal domain was adopted, although the methodology itself is not restricted to a particular identification method. The whole approach is applied to experimental data related to a very thin beam exhibiting a distributed nonlinear behavior. Results show a very good level of accuracy validating the effectiveness of the methodology. Further improvements should take into account also nonlinear damping and the possibility to test the method on more complex real-life structures exhibiting large deformations.

References

[1] A.H. Nayfeh, P.F. Pai, Linear and nonlinear structural mechanics, 2004. doi:10.1007/s11012-005-0327-y.

[2] F. Wenneker, P. Tiso, A substructuring method for geometrically nonlinear structures, Conf. Proc. Soc. Exp. Mech. Ser. 1 (2014) 157–165. doi:10.1007/978-3-319-04501-6_14.

[3] M. Amabili, M.P. Païdoussis, Review of studies on geometrically nonlinear vibrations and dynamics of circular cylindrical shells and panels, with and without fluid-structure interaction, Appl. Mech. Rev. 56 (2003) 349. doi:10.1115/1.1565084.

[4] M. Sathyamoorthy, Nonlinear analysis of structures, CRC Press, New York, 1998.

[5] C. Touzé, O. Thomas, A. Huberdeau, Asymptotic non-linear normal modes for large-amplitude vibrations of continuous structures, Comput. Struct. 82 (2004) 2671–2682. doi:10.1016/j.compstruc.2004.09.003.

[6] C.S.M. Sombroek, P. Tiso, L. Renson, G. Kerschen, Numerical computation of nonlinear normal modes in a modal derivative subspace, Comput. Struct. 195 (2018) 34–46. doi:10.1016/j.compstruc.2017.08.016.

[7] G. Kerschen, K. Worden, A.F. Vakakis, J.C. Golinval, Past, present and future of nonlinear system identification in structural dynamics, Mech. Syst. Signal Process. 20 (2006) 505–592. doi:10.1016/j.ymssp.2005.04.008.

[8] J.P. Noël, G. Kerschen, Nonlinear system identification in structural dynamics: 10 more years of progress, Mech. Syst. Signal Process. 83 (2017) 2–35. doi:10.1016/j.ymssp.2016.07.020.

[9] M. Claeys, J.J. Sinou, J.P. Lambelin, B. Alcoverro, Multi-harmonic measurements and numerical simulations of nonlinear vibrations of a beam with non-ideal boundary conditions, Commun. Nonlinear Sci. Numer. Simul. 19 (2014) 4196–4212. doi:10.1016/j.cnsns.2014.04.008.

[10] X. Wang, T.L. Hill, S.A. Neild, Frequency response expansion strategy for nonlinear structures, Mech. Syst. Signal Process. 116 (2019) 505–529. doi:10.1016/j.ymssp.2018.06.027.

[11] D. Piombino, M.S. Allen, D. Ehrhardt, T. Beberniss, J.J. Hollkamp, System identification to estimate the nonlinear modes of a gong, Conf. Proc. Soc. Exp. Mech. Ser. 1 (2019) 121–136. doi:10.1007/978-3-319-74280-9_10.

[12] S. Marchesiello, L. Garibaldi, A time domain approach for identifying nonlinear vibrating structures by subspace methods, Mech. Syst. Signal Process. 22 (2008) 81–101. doi:10.1016/j.ymssp.2007.04.002.

[13] J.P. Noël, G. Kerschen, Frequency-domain subspace identification for nonlinear mechanical systems, Mech. Syst. Signal Process. 40 (2013) 701–717. doi:10.1016/j.ymssp.2013.06.034.

[14] J.P. Noël, S. Marchesiello, G. Kerschen, Subspace-based identification of a nonlinear spacecraft in the time and frequency domains, Mech. Syst. Signal Process. 43 (2014) 217–236. doi:10.1016/j.ymssp.2013.10.016.

[15] D.E. Adams, R.J. Allemang, Frequency domain method for estimating the parameters of a non-linear structural dynamic model through feedback, Mech. Syst. Signal Process. 14 (2000) 637–656. doi:10.1006/mssp.2000.1292.

[16] L. Meirovitch, Principles and techniques of vibrations, Prentice Hall, 1997.

[17] S. Jain, P. Tiso, J.B. Rutzmoser, D.J. Rixen, A quadratic manifold for model order reduction of nonlinear structural dynamics, Comput. Struct. 188 (2017) 80–94. doi:10.1016/j.compstruc.2017.04.005.

[18] P. Van Overschee, B. De Moor, Subspace Identification for Linear Systems, Springer US, Boston, MA, 1996. doi:10.1007/978-1-4613-0465-4.

[19] T. McKelvey, H. Akçay, L. Ljung, Subspace-based multivariable system identification from frequency response data, IEEE Trans. Automat. Contr. (1996). doi:10.1109/9.508900.

[20] G. De Filippis, J.P. Noël, G. Kerschen, L. Soria, C. Stephan, Model reduction and frequency residuals for a robust estimation of nonlinearities in subspace identification, Mech. Syst. Signal Process. 93 (2017) 312–331. doi:10.1016/j.ymssp.2017.01.020.

[21] P.F. Pai, A.H. Nayfeh, Non-linear non-planar oscillations of a cantilever beam under lateral base excitations, Int. J. Non. Linear. Mech. 25 (1990) 455–474. doi:10.1016/0020-7462(90)90012-X.

[22] A.Y.T. Leung, S.G. Mao, A symplectic Galerkin method for non-linear vibration of beams and plates, J. Sound Vib. 183 (1995) 475–491. doi:10.1006/jsvi.1995.0266.

[23] V. Sonneville, A. Cardona, O. Brüls, Geometrically exact beam finite element formulated on the special Euclidean group SE(3), Comput. Methods Appl. Mech. Eng. 268 (2014) 451–474. doi:10.1016/j.cma.2013.10.008.

[24] J. Chung, G.M. Hulbert, A Time Integration Algorithm for Structural Dynamics With Improved Numerical Dissipation: The Generalized-α Method, J. Appl. Mech. (1993). doi:10.1115/1.2900803.

[25] R. Pintelon, J. Schoukens, System Identification: A Frequency Domain Approach, Second Edition, 2012. doi:10.1002/9781118287422.

[26] J. Schoukens, M. Vaes, R. Pintelon, Linear System Identification in a Nonlinear Setting: Nonparametric Analysis of the Nonlinear Distortions and Their Impact on the Best Linear Approximation, IEEE Control Syst. 36 (2016) 38–69. doi:10.1109/MCS.2016.2535918.

[27] S. Marchesiello, A. Fasana, L. Garibaldi, Modal contributions and effects of spurious poles in nonlinear subspace identification, Mech. Syst. Signal Process. 74 (2016) 111–132. doi:10.1016/j.ymssp.2015.05.008.